

The Impact of Environment on Late-time Evolution of the Stellar Mass-Halo Mass Relation

Jesse B. Golden-Marx ¹ and Christopher J. Miller ^{1,2}

Department of Astronomy, University of Michigan, Ann Arbor, MI 48109 USA; jessegm@umich.edu

Department of Physics, University of Michigan, Ann Arbor, MI 48109, USA

Received 2019 January 8; revised 2019 April 8; accepted 2019 April 25; published 2019 June 7

Abstract

At a fixed halo mass, galaxy clusters with larger differences in brightness between the brightest central galaxy (BCG) and fourth-brightest cluster member ($m_{\rm gap}$) have larger BCG stellar masses. Recent studies have shown that by including $m_{\rm gap}$ as a latent parameter in the cluster stellar mass—halo mass (SMHM) relation, one can make more precise measurements of the SMHM relation's amplitude, slope, and intrinsic scatter. We use galaxy clusters from the Sloan Digital Sky Survey to measure the SMHM— $m_{\rm gap}$ relation and its evolution out to z=0.3. Using a fixed comoving aperture of 100 kpc to define the central galaxy's stellar mass, we report statistically significant negative evolution in the slope of the SMHM relation to z=0.3 (>3.5 σ). The steepening of the slope over the past 3.5 Gyr can be explained by late-time merger activity at the cores of galaxy clusters. We also find that the inferred slope depends on the aperture used to define the radial extent of the central galaxy. At small radii (20 kpc), the slope of the SMHM relation is shallow, indicating that the core of the central galaxy is less related to the growth of the underlying host halo. By including all of the central galaxy's light within 100 kpc, the slope reaches an asymptote value.

Key words: galaxies: clusters: general – galaxies: elliptical and lenticular, cD – galaxies: evolution

1. Introduction

The stellar mass-halo mass (SMHM) relation is one of the primary mechanisms used to quantify the galaxy-dark matter halo connection. For clusters $(\log_{10}(M_{\rm halo}/(h^{-1}M_{\odot})) \geqslant 14.0)$, this linear relation relates the stellar mass of the brightest central galaxy (BCG) to the total cluster halo mass, including the dark matter. The inferred intrinsic scatter $(\sigma_{\rm int})$ associated with this relation can be used to constrain the processes that quench star formation within galaxies (Tinker 2017) and characterize the growth of their massive, underlying, dark matter halos (Gu et al. 2016).

BCGs, the stellar mass portion of the cluster-scale SMHM relation, are massive, extended, luminous elliptical galaxies that account for a significant fraction of light emitted from their host cluster halos (e.g., Schombert 1986; Jones et al. 2000; Lin & Mohr 2004; Bernardi et al. 2007; Lauer et al. 2007; von der Linden et al. 2007; Aguerri et al. 2011; Brough et al. 2011; Proctor et al. 2011; Harrison et al. 2012). Unlike other cluster members, their location near the X-ray center of the cluster leads to their properties correlating with that of their host cluster halo (Jones & Forman 1984; Rhee & Latour 1991; Lin & Mohr 2004; Lauer et al. 2014). The current theory of BCG formation is the two-phase formation scenario, where a dense core forms at high redshifts via in situ star formation and the outer portions of the BCG grow as a result of the hierarchical merging of satellite galaxies (Oser et al. 2010). This theory is well supported by observations (van Dokkum et al. 2010; Huang et al. 2018) and dark-matter-only cosmological simulations that use semiempirical or semi-analytic prescriptions for the stellar mass growth of central galaxies (e.g., Croton et al. 2006; De Lucia & Blaizot 2007; Guo et al. 2011; Tonini et al. 2012; Shankar et al. 2015).

One observational measurement intrinsically tied to the stellar mass growth of the BCG is the magnitude gap $(m_{\rm gap})$, the difference in the r-band magnitude between the BCG and either

the second-brightest (M12) or fourth-brightest (M14) cluster member within half of the radius that encloses 200× the critical density of the universe (R_{200} ; Jones et al. 2003; Dariush et al. 2010). For the purpose of this paper, we use the fourth-brightest member, since it best identifies early forming clusters (Dariush et al. 2010). Based on dissipationless simulations of young and previrialized groups, Solanes et al. (2016) find that the stellar mass of the central galaxy linearly increases with the number of progenitor galaxies, in agreement with hierarchical growth. Furthermore, BCGs grow at the expense of the second-brightest galaxy. Thus, as the BCG merges with the surrounding fainter galaxies, the stellar mass and magnitude of the BCG increase, relative to the second- or fourth-brightest galaxy, increasing $m_{\rm gap}$. Therefore, $m_{\rm gap}$ is a latent third parameter in the cluster SMHM relation as shown in Golden-Marx & Miller (2018, hereafter GM&M18).

GM&M18 incorporate $m_{\rm gap}$ and alter the cluster-scale SMHM relation from

$$\log_{10}(M_*) = \alpha + \beta \log_{10}(M_{\text{halo}}) \tag{1}$$

to

$$\log_{10}(M_*) = \alpha + \beta \log_{10}(M_{\text{halo}}) + \gamma M 14, \tag{2}$$

where α is the offset, β is the slope, γ is the $m_{\rm gap}$ stretch parameter, and M14 is the selected $m_{\rm gap}$. These parameters are measured for the Sloan Digital Sky Survey (SDSS) C4 cluster sample ($\log_{10}(M_{\rm halo}/(h^{-1}M_{\odot})) \geqslant 14.0$; Miller et al. 2005) with caustic halo masses (Gifford et al. 2013) using a hierarchical Bayesian MCMC analysis. Incorporating γ into the SMHM relation reduces the inferred intrinsic scatter and uncertainties on the amplitude and slope of the SMHM relation (GM&M18).

BCGs grow hierarchically; therefore, the slope of the SMHM relation may change over time because at higher redshifts fewer mergers will have occurred and the stellar mass of the BCG will be lower (Solanes et al. 2016). Moreover, dark

matter halos are thought to grow hierarchically, as smaller subhalos merge with the cluster halo over time, so the average halo mass should also decrease (White & Rees 1978; Springel et al. 2005; De Lucia & Blaizot 2007).

The redshift evolution of the SMHM relation has been investigated using observations, empirical models, and simulations. Observationally, Oliva-Altamirano et al. (2014) use BCGs and brightest group galaxies from the Galaxy and Mass Assembly survey and find no evolution in the SMHM relation's slope over the redshift range 0.1 < z < 0.3, while Gozaliasl et al. (2016) use a sample of X-ray-selected galaxy groups and find that the SMHM relation's slope does not evolve over the redshift range 0.1 < z < 1.3. Using empirical models and abundance matching techniques to infer halo masses, Behroozi et al. (2013) and Moster et al. (2013) find that the slope evolves by 40%–50% from z = 0.0 to z = 1.0. Moster et al. (2013) also find moderate evolution out to just z = 0.5. In contrast, Pillepich et al. (2018) use the Illustris TNG300 cosmological hydrodynamical simulation and report little change in the slope between z = 0.0 and z = 1.0. In addition to the redshift evolution in the slope of the SMHM relation, the evolution of the intrinsic scatter has also been investigated using hydrodynamical simulations (Matthee et al. 2017; Pillepich et al. 2018), N-body simulations (Gu et al. 2016), and empirical models (Behroozi et al. 2019; Moster et al. 2018). However, the results from these different approaches are inconsistent with one another and may depend on the initial conditions of the simulations. The most likely reason no consensus exists for the redshift evolution of the intrinsic scatter and SMHM relation slope is due to differences in how the stellar and halo masses, as well as the associated uncertainties, are estimated in simulations, empirical models, and observations.

As previously noted, including $m_{\rm gap}$ as a latent parameter in the SMHM relation allows other parameters, such as the slope, to be measured with higher precision. Thus, Equation (2) plays a critical role in detecting redshift evolution of the SMHM relation. One can also allow the stretch parameter to evolve, which may provide information about the BCG merger history and the fraction of stellar matter from major and minor mergers that ends up as part of the intracluster light (ICL) that surrounds the BCG.

The outline for the remainder of this paper is as follows. In Section 2, we summarize the goals, methods, and results of GM&M18. In Section 3, we discuss the observations and simulated data used to measure stellar masses, halo masses, and $m_{\rm gap}$ values for our SMHM relation. In Section 4, we describe the hierarchical Bayesian MCMC model used to evaluate the redshift evolution of the SMHM relation. In Section 5, we describe how we use the low-redshift data to calibrate the higher-redshift clusters and their observational errors. In Section 6, we present our results. In Section 7 we discuss our findings and conclude.

Except for the case of simulated data, in which the cosmological parameters are previously defined (Springel et al. 2005), for our analysis we assume a flat Λ CDM universe, with $\Omega_M=0.30,~\Omega_\Lambda=0.70,~{\rm and}~H=100~h~{\rm km\,s^{-1}\,Mpc^{-1}}$ with h=0.7.

2. Summary of Golden-Marx & Miller (2018)

Many of the analyses in this paper build on GM&M18, so we briefly summarize those results. GM&M18 set out to explain the discrepancy between amplitudes of previously published SMHM

relations using the low-redshift SDSS-C4 (Miller et al. 2005) sample of clusters ($z_{\rm med}=0.086$). BCG Petrosian magnitudes were properly corrected for known SDSS background subtraction issues, and stellar masses were determined using the Bell et al. (2003) mass-to-light ratio (M/L) conversion. Halo masses were measured individually for each cluster using the caustic technique (e.g., Gifford et al. 2013). $m_{\rm gap}$ was measured using red sequence cluster members within 0.5 $R_{\rm vir}$ and introduced as a third parameterized variable in the linear SMHM relation. GM&M18 termed this third parameter the "stretch" parameter (γ) and found it to be nonzero with high statistical significance. GM&M18 also showed that $m_{\rm gap}$ plays an equally important role in the SMHM relation from semi-analytic galaxy catalogs, suggesting that it stems naturally from hierarchical growth (Guo et al. 2011; Henriques et al. 2012).

To achieve their results, GM&M18 developed a hierarchical Bayesian model that accounts for errors on all observables, including the intrinsic uncertainty in stellar mass at fixed halo mass ($\sigma_{\rm int}$). The model also incorporates a level of uncertainty on the estimated errors. GM&M18 used simulated light-cone data based on the Millennium Simulation (Henriques et al. 2012) to test the model and its ability to accurately recover the true underlying SMHM– $m_{\rm gap}$ parameters using only projected measurements (e.g., projected dynamical cluster masses, projected $m_{\rm gap}$ values, and stellar masses inferred from galaxy magnitudes). In this new work, we use the same model, except that we add parameters to allow for redshift evolution in the amplitude, slope, stretch, and intrinsic scatter.

GM&M18 showed that the majority of the discrepancies in the reported amplitude of the cluster-scale SMHM can be explained by simply accounting for $m_{\rm gap}$ in the cluster sample selection. GM&M18 also noted that the inferred errors on the parameters in the SMHM relation, as well as $\sigma_{\rm int}$, are significantly reduced (by as much as a factor of 2) after incorporating $m_{\rm gap}$ into the SMHM model.

3. Data

The observational data used for this analysis come from SDSS DR8 (Aihara et al. 2011) and DR12 (Alam et al. 2015). For the full cluster sample, we combine the SDSS-C4 (Miller et al. 2005) sample used in GM&M18 with v6.3 of the SDSS-redMaPPer catalog (Rykoff et al. 2014). The SDSS-C4 cluster sample used in GM&M18 is highly complete from $0.03 \le z \le 0.1$, while redMaPPer has high completeness over the range $0.10 \le z \le 0.35$ (Groenewald et al. 2017). Since we are studying redshift evolution, we want our final sample of clusters to cover the widest possible redshift range. Therefore, we need to make measurements of halo masses, $m_{\rm gap}$ values, and BCG stellar masses for SDSS-C4 and redMaPPer clusters in a homogeneous fashion.

3.1. redMaPPer m_{gap}

The redMaPPer algorithm is a red-sequence-based photometric cluster-finding algorithm. The redMaPPer red sequence model was constructed using a sample of spectroscopically confirmed clusters. Using this calibrated model, clusters are identified using luminosity and radial filters. redMaPPer also assigns a membership probability for cluster member galaxies, $P_{\rm mem}$, which depends on the richness, cluster density profile, and background density. According to Rykoff et al. (2014), if $P_{\rm mem} > 0.70$, a galaxy should be considered a member. These

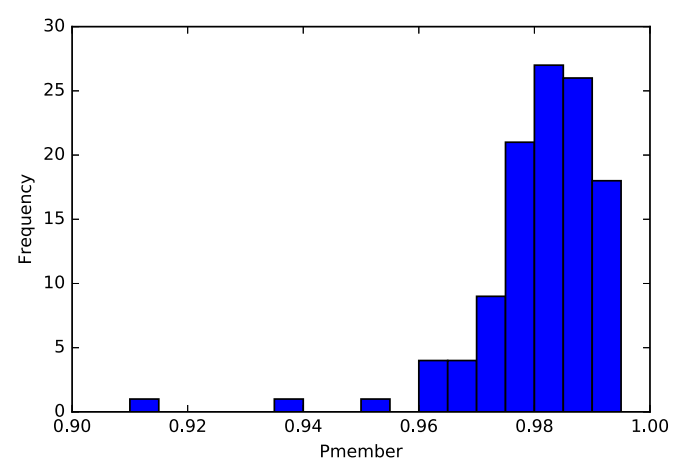


Figure 1. Distribution of the $P_{\rm mem}$ values required to match the number of cluster members brighter than r=18.0 in the SDSS-C4 and redMaPPer baseline sample. The median value is $P_{\rm mem}=0.984$.

high-probability members are then used to estimate photometric redshifts, which we use in our Bayesian MCMC analysis (Section 4.2). redMaPPer provides a probability for being the central galaxy for the five most likely candidate centrals, and we identify the BCG as the most likely candidate.

Galaxy membership in the SDSS-C4 sample (GM&M18) differs from the redMaPPer sample owing to color selection and sky apertures. SDSS-C4 cluster members are identified using individual cluster red sequences in six distinct SDSS colors (u–g, g–r, g–i, r–i, i–z, and r–z), which are fit using all potential cluster member galaxies with an r-band magnitude brighter than m_r = 19 within 0.5 $R_{\rm vir}$ of the BCG, where $R_{\rm vir}$ is estimated using the caustic halo mass. We note that this includes two additional colors compared to the SDSS-C4 cluster-finding algorithm (Miller et al. 2005). Cluster members are those galaxies simultaneously within 3 σ of the red sequence for the u–g, g–r, and g–i colors and 2 σ for the r–i, i–z, and r–z colors (GM&M18). The SDSS-C4 BCGs are visually confirmed and are identified as being the brightest in the red sequence.

We calibrate the redMaPPer $m_{\rm gap}$ values to the SDSS-C4 $m_{\rm gap}$ measurements, where for both samples the fourth brightest is chosen from within the red sequence. To calibrate these samples, we need to homogenize the membership of the clusters in color–magnitude space. As noted earlier, redMaPPer membership depends on a specified $P_{\rm mem}$ threshold. We determine this threshold using 112 clusters found in both catalogs. For these clusters, we match the density of galaxies within color–magnitude space between SDSS-C4 and red-MaPPer by adjusting the latter's $P_{\rm mem}$ threshold. As we adjust $P_{\rm mem}$ and the sky aperture size, we can raise or lower the number of galaxies in the color–magnitude diagrams of the redMaPPer clusters.

We use only galaxies within an estimate of $0.5 \times R_{\text{virial}} \sim 0.5 \times R_{200}$. Although redMaPPer does not provide R_{200} , we can approximate R_{200} using Equation (3) from Rykoff et al. (2014),

$$R_{200} \approx 1.5 R_c(\lambda),$$
 (3)

where λ is the redMaPPer cluster richness and R_c is the redMaPPer cutoff radius, given by

$$R_c(\lambda) = 1.0h^{-1}\text{Mpc}(\lambda/100)^{0.2}.$$
 (4)

Figure 1 shows that a median value of $P_{\text{mem}} = 0.984$ matches the two membership definitions with good precision.

Therefore, we apply this $P_{\rm mem}$ threshold when identifying cluster members used to determine $m_{\rm gap}$ for the redMaPPer sample. We note that when we examine how the number of members changes as a function of $P_{\rm mem}$, we observe little change in the range $0.7 < P_{\rm mem} < 0.9$ but large decreases in membership at $P_{\rm mem} > 0.9$.

Unlike in GM&M18, we no longer use Petrosian magnitudes. Instead, we measure $m_{\rm gap}$ as the difference between the k-corrected r-band model magnitudes of the BCG and fourth-brightest cluster member. Applying our restrictive cluster member criterion and using the model magnitudes, we find good agreement in the distribution of $m_{\rm gap}$ values for the overlapping redMaPPer and SDSS-C4 clusters. We discuss the errors on the $m_{\rm gap}$ measurements in Section 5.

3.2. redMaPPer Halo Mass

To determine halo masses for the redMaPPer sample, we use the mass-richness relation from Simet et al. (2017), given by

$$M_{\text{halo}}/(h^{-1}M_{\odot}) = 10^{14.344} (\lambda/40)^{1.33}.$$
 (5)

Here λ is the standard redMaPPer richness, or galaxy count as given in Rykoff et al. (2014). The minimum redMaPPer richness we use is >22, depending on the minimum mass threshold applied.

In GM&M18, we used individual dynamically inferred cluster masses from the caustic technique (Gifford et al. 2013). However, to homogenize the analysis between the low-z SDSS-C4 and redMaPPer clusters, we require a mass–richness relation for the SDSS-C4 sample. For both samples, we need an estimate of the intrinsic scatter in mass at a fixed richness, which is discussed in Section 5.

3.3. Final redMaPPer Sample

We analyze the redshift evolution of the SMHM relation in two ways. First, we bin our data by redshift and determine the posteriors from our Bayesian MCMC model for each bin with the redshift evolution parameters set to 0.0, and second, we incorporate redshift evolution using four additional parameters in Equation (2) and fit against all of the redMaPPer clusters. For this analysis, we look at the redshift range $0.08 \leqslant z \leqslant 0.30$, where redMaPPer is suggested to be most complete (Groenewald et al. 2017) and we have enough clusters for a statistically significant sample.

The total sample of 1005 redMaPPer clusters with stellar masses measured out to 100 kpc, with greater than four members with $P_{\rm mem} \geqslant 0.984$ within $0.5R_{200}$, and within $0.08 \leqslant z \leqslant 0.3$ has no mass limit applied. However, we do not expect the redMaPPer sample to have the same lower mass limit throughout this redshift range, and we must also check for $m_{\rm gap}$ incompleteness since SDSS is a flux-limited survey.

Therefore, the redMaPPer sample was divided into four redshift bins, each initially with \sim 251 clusters. For each bin, as done in GM&M18, we use an $m_{\rm gap}$ completeness analysis where we bin the absolute magnitude of the BCG and fourth-brightest member against both the BCG's apparent magnitude and $m_{\rm gap}$ to determine the apparent magnitude limit of the sample (a redshift-dependent limit; Colless 1989; Garilli et al. 1999; La Barbera et al. 2010; Trevisan et al. 2017; Golden-Marx & Miller 2018).

To account for halo mass incompleteness, for each redshift bin, the halo mass distribution can be approximated as a Gaussian, where the peak indicates the mass at which the sample starts to become incomplete. Instead of applying a model-dependent correction to the analysis, we apply a lower halo mass cut where the amplitude of the binned halo mass distribution decreases to 70% of the peak value to ensure high completeness as a function of redshift. This is a conservative choice that results in a redMaPPer richness threshold of \sim 22, well above the detection limit for the redMaPPer algorithm. However, when combined with the $m_{\rm gap}$ completeness analysis, these cuts shrink our available sample down to 843 clusters, a reduction of \sim 16%. A slightly more restrictive (higher) halo mass lower limit has no effect on our final results.

Since we study clusters out to z = 0.3, where the SDSS-redMaPPer sample is volume limited, we do not apply any corrections for volume effects from Malmquist bias.

3.4. SDSS-C4 Sample and Richness-based Halo Masses

The SDSS-C4 clusters are nearly identical to those used in GM&M18. The samples differ because the stellar masses are estimated, as described in Section 3.5, within 100 kpc, instead of within the Petrosian radius. Additionally, we use a mass-richness relation to infer the redMaPPer halo masses. Therefore, instead of the individual dynamical cluster masses, we also use a mass-richness relation for the SDSS-C4 sample. For this analysis, we use only clusters with clean phase spaces to ensure that our richness measurement is meaningful and unimpacted by foreground and background contamination. Given these individual masses and the observed galaxy and background counts, we make a preliminary constraint on the SDSS-C4 mass-richness relation using techniques similar to Andreon & Hurn (2010). We find

$$M_{\text{halo}}/(h^{-1}M_{\odot}) = 10^{14.195} (\lambda^{C4}/33.1)^{1.134}.$$
 (6)

We note that the richnesses (λ^{C4}) for the SDSS-C4 sample are not calculated in the same manner as the redMaPPer richnesses. However, using the sample of clusters found in both SDSS-C4 and SDSS-redMaPPer, we find that the offset between the redMaPPer and C4 mass estimates is 0.1 dex, with a standard devation of 0.15 dex. As shown in Table 2, when this offset is removed, the results of our analysis do not change. A more detailed analysis of the SDSS-C4 mass-richness relation will be presented elsewhere (C. J. Miller et al. 2019, in preparation). Using this mass-richness relation, we apply the mass limits of $14.0 \leq \log_{10}(M_{\text{halo}}/(h^{-1}M_{\odot})) \leq 14.7$. The upper limit was selected to eliminate Malmquist bias in the low-redshift (and small-volume) sample. Overall, these changes result in a sample of 142 clusters with clean richnesses used in this analysis.

3.5. BCG Stellar Masses

In GM&M18, we emphasized the importance of correcting the BCG magnitudes because of the SDSS background subtraction error (Bernardi et al. 2007, 2013; von der Linden et al. 2007; Harrison et al. 2012). This correction is a strong function of the apparent size of the galaxies and is especially problematic at low redshifts. The BCGs in redMaPPer are smaller in their apparent sizes and suffer much less from the known issues of the background light subtraction compared to the SDSS-C4 sample (Bernardi et al. 2007; von der Linden et al. 2007; Harrison et al. 2012; Golden-Marx & Miller 2018), so we do not need to remeasure the BCG light profiles to

correct for missed light within selected radii of the BCGs and include additional uncertainties on the BCG stellar mass estimates. Instead, we use the stellar mass measured within a fixed and precise 100 kpc radial extent, a choice that is justified in Section 5.1, which results in a much smaller uncertainty on the stellar masses. To measure the 100 kpc magnitudes, we queried the SDSS DR12 (Alam et al. 2015) database to obtain the SDSS azimuthally averaged radial light profile for each BCG and then integrated these profiles to 100 kpc.

To calculate BCG stellar masses, unlike in GM&M18, we do not use the Bell et al. (2003) M/L to estimate stellar mass because this relation is calibrated for z=0.0. Instead, we use the EzGal spectral energy distribution (SED) modeling software (Mancone & Gonzalez 2012) to estimate stellar mass. We note that GM&M18 found no differences in their fits to the SMHM relation when using the EzGal-based stellar masses versus the stellar masses estimated using Bell et al. (2003).

When estimating stellar masses using EzGal, we use a Bruzual & Charlot (2003) stellar population synthesis model, a Salpeter (1955) initial mass function, a formation redshift of z = 4.9, and a constant metallicity of 0.4 z_{\odot} . We apply a Bayesian MCMC approach, done in emcee (Foreman-Mackey et al. 2013). We treat the absolute magnitude (the normalization parameter selected for EzGal) as a free parameter, with a uniform prior, to determine the absolute magnitude that minimizes the chi-squared between the EzGal modeled g-, r-, and i-band magnitudes measured at the observed redshift and the SDSS g-, r-, and i-band magnitudes measured at 100 kpc. We note that initially metallicity was treated as a free parameter. However, \approx 99% had a minimum chi-squared when the metallicity of 0.4 z_{\odot} was chosen, so we removed this free parameter. Using this approach, we estimate the stellar mass uncertainty to be 0.08 dex, consistent with the suggestion from Bell et al. (2003). This is about half the uncertainty used in GM&M18, where the precision in determining the Petrosian radius and the induced error from the background correction dominate the error budget.

3.6. Simulated Data

In addition to studying the evolution of the SMHM– $m_{\rm gap}$ relation in the SDSS-C4 and redMaPPer data, we also analyze the same trend using the Guo et al. (2011) prescription of the semi-analytic representations of low-redshift clusters in the Millennium Simulation. Unlike in GM&M18, we do not use the Henriques et al. (2012) prescription because it is magnitude limited to $K_s \approx 21.8$, which at z=0.3 corresponds to $r\approx 18$, far fainter than that of our observed sample. Also, the periodic replications within Henriques et al. (2012) may introduce additional, unaccounted-for noise in our MCMC model. For this analysis, we use the Guo et al. (2011) simulation boxes analyzed at redshifts of 0.089, 0.116, 0.144, 0.174, and 0.242, the redshifts that best match our binned sample and correspond to snapshot numbers 59, 58, 57, 56, and 54.

For the simulated data analysis we use the 3D information provided directly from the Guo et al. (2011) prescription of the Millennium Simulation for each cluster, which includes halo masses, measured within $R_{200} \times \rho_{\rm crit}$; the galaxy positions, x, y, z; R_{200} ; the semi-analytic stellar masses; and the magnitudes. To determine cluster membership, we use the positional information (x, y, z) to determine whether potential cluster members are within $0.5R_{200}$. For those galaxies within this sphere, we identify galaxies within 2 standard deviations from the red sequence as cluster members. M14 is then measured as

the difference between the fourth-brightest member and BCG in the r band. Since the BCG stellar masses are provided by the Guo et al. (2011) prescription of the Millennium Simulation and we have access to the entire simulation box, we do not apply a completeness criterion to our simulated sample for each redshift bin. However, to make our samples comparable, we apply the halo mass distribution function of the binned SDSSredMaPPer data to the simulation snapshot at the corresponding redshift.

4. The Hierarchical Bayesian Model

We use a hierarchical Bayesian MCMC analysis to determine the values of α , β , γ , σ_{int} , and the redshift evolution parameters given in Equation (7). The Bayesian approach can be described as convolving prior information for a given model with the likelihood of the observations given the model to yield the probability of observing the data given the model, or the posterior distribution up to a normalization constant called the Bayesian evidence.

To generate the posterior distributions for each of the parameters, our MCMC model generates values for the observed stellar masses, halo masses, and $m_{\rm gap}$ values at each step in our likelihood analysis, which are then directly compared to the observed measurements. As described in Section 2, we modified our previous MCMC model (GM&M18) to improve the speed of convergence. Our new model is summarized below.

4.1. Bayesian Model Incorporating Redshift Evolution

4.1.1. The Observed Quantities

For our redshift evolution model, we use similar equations and relations to quantify the observed or measured values for the halo mass and m_{gap} and the same relation for stellar mass as described in GM&M18. The log_{10} BCG stellar masses (y), \log_{10} halo masses (x), and M14 values (z) are modeled as being drawn from Gaussian distributions with mean values (locations) taken from the observed data. The standard deviations are the errors on each measurement and include an estimate of the observational uncertainty $(\sigma_{x_0}, \sigma_{y_0}, \sigma_{z_0})$ and an additional stochastic component from a beta function $\beta(0.5,100)$ (GM&M18), which allows for realistic uncertainty on the observational errors. These are treated statistically in the Bayesian model as free nuisance parameters σ_x , σ_y , and σ_z .

One modification we made to the likelihood and prior from GM&M18 is that we no longer model the underlying halo mass and $m_{\rm gap}$ distributions as truncated normal distributions; instead, we use a Gaussian distribution and allow the halo mass values for any step of the trace to be below our lower limit. However, the median halo mass of each cluster generated in the MCMC chains reflects the halo mass lower limit listed in Table 3.

4.2. The Unobserved Quantities

The new version of this model incorporates redshift evolution through parameters on α , β , γ , and σ_{int} . As in GM&M18, we are only concerned with the cluster portion of the SMHM relation, which is modeled linearly. As such,

Equation (2) becomes

$$y_i = \alpha (1 + z_{\text{red}})^{n_1} + (\beta (1 + z_{\text{red}})^{n_2}) x_i + (\gamma (1 + z_{\text{red}})^{n_3}) z_i.$$
(7)

In Equation (7), z_{red} is the photometric redshift determined via red sequence fitting from redMaPPer (Rykoff et al. 2014) or the spectroscopic redshift for the SDSS-C4 clusters, not to be confused with z, the shorthand for the $m_{\rm gap}$, M14. We assume a Gaussian likelihood form, with an intrinsic scatter that can also evolve with redshift: $\sigma_{\rm int}(1+z_{\rm red})^{n_4}$. The four parameters, n_1 , n_2 , n_3 , and n_4 , measure the redshift evolution of α , β , γ , and $\sigma_{\rm int}$, respectively. When we use this model for the redshift binned sample described in Section 3.3, these parameters are set to 0.0, which reduces Equation (7) to Equation (2). This means that the zero redshift model used in GM&M18 is nested within our new model. By using nested models, we can interpret how much better a given model is (e.g., with redshift evolution vs. without) using only the posterior distribution.

Our Bayesian model regresses against the observed stellar mass, halo mass, and $m_{\rm gap}$ values simultaneously and selfconsistently. We treat parameters that model the underlying distributions and their uncertanties as nuisance parameters, and we marginalize over them when we present the posterior distributions in Section 6.1. All parameters in the Bayesian analysis are presented in Table 1 along with their priors. We discuss the strong priors on the observed uncertainties in Section 5.

We can express the entire posterior as

$$p(\alpha, \beta, \gamma, \sigma_{int}, n_1, n_2, n_3, n_4, x_i, z_i, \sigma_{y_i}, \sigma_{z_i}) \propto \underbrace{P(y_{0i} | \alpha, \beta, \gamma, \sigma_{y_i}, n_1, n_2, n_3, n_4, \sigma_{int}, x_i, z_i) P(x_{0i} | x_i, \sigma_{x_i}) P(z_{0i} | z_i, \sigma_{z_i})}_{\text{likelihood}} \underbrace{P(x_i) p(z_i) p(\sigma_{x_i}) p(\sigma_{y_i}) p(\sigma_{z_i}) p(\alpha) p(\beta) p(\gamma) p(\sigma_{int}) p(n_1, n_2, n_3, n_4)}_{\text{priors}},$$

(8)

where each ith cluster is a component in the summed log likelihood.

Like the model presented in GM&M18, we use a hierarchical Bayes model because the priors on the true halo masses (x_i) and M14 values (z_i) depend on models themselves (the observed halo mass and M14 distributions).

5. Calibration

For this paper, we study a larger sample out to a higher redshift ($z \le 0.3$) than in the SDSS-C4 sample ($z_{\text{med}} = 0.086$). The larger sample allows us to reduce the statistical noise in the data, while the higher redshift allows us to search for late-time evolution in the SMHM relation (i.e., in the past \sim 3.5 Gyr). Two important trade-offs when using the bigger and deeper red-MaPPer data combined with the lower-redshift SDSS-C4 data are that we need to calibrate the observables (see Section 3) and that we have less secure mean values of the observational uncertainties, such as the $m_{\rm gap}$ values and the halo masses.

5.1. Aperture Radius and the Slope of the SMHM Relation

Because we are studying redshift evolution, we need to use a BCG aperture for the stellar masses that is unbiased owing to the decrease in apparent size and signal-to-noise ratio of the

Table 1
Bayesian Analysis Parameters for the Combined SDSS-C4 and SDSS-redMaPPer Sample

Symbol	Description	Prior
α	The offset of the SMHM relation	U(-20, 20)
β	The high-mass power-law slope	Linear regression prior
γ	The stretch parameter, which describes the stellar mass-M14 stratification	Linear regression prior
$\sigma_{ m int}$	The uncertainty in the intrinsic stellar mass at fixed halo mass	U(0.0, 0.5)
y_i	The underlying distribution in stellar mass	Equation (7)
x_i	The underlying halo mass distribution	$\mathcal{N}(14.28, 0.22^2)$
z_i	The underlying $m_{\rm gap}$ distribution	$\mathcal{N}(2.13, 0.57^2)$
n_1	The power law associated with the redshift evolution of α	$\mathcal{U}(-10.0, 10.0)$
n_2	The power law associated with the redshift evolution of β	U(-10.0, 10.0)
n_3	The power law associated with the redshift evolution of γ	U(-10.0, 10.0)
n_4	The power law associated with the redshift evolution of σ_{int}	U(-20.0, 20.0)
$\sigma_{y_{0i}}$	The uncertainty between the observed stellar mass and intrinsic stellar mass distribution	0.08 dex
$\sigma_{x_{0i}}$	The uncertainty associated with the mass-richness relation	0.087 dex
$\sigma_{z_{0i}}$	The uncertainty between the underlying and observed $m_{\rm gap}$ distribution	0.15

Note. U(a, b) refers to a uniform distribution, where a and b are the upper and lower limits, respectively. The linear regression prior is of the form $-1.5 \times \log(1 + \text{value}^2)$. $\mathcal{N}(a, b)$ refers to a normal distribution with mean and variance of a and b. Additionally, we note that for x_i and z_i the means and widths given in this table are example values belonging to the lowest SDSS-redMaPPer redshift bin.

galaxies out to z = 0.3. Since we expect little physical growth in BCGs over this redshift range, we choose a fixed kiloparsec aperture.

Zhang et al. (2016), using DES science verification data, measure the slope of the SMHM relation using photometry measured within four radial extents ranging from 15 to 60 kpc and stellar masses estimated using EzGal (Mancone & Gonzalez 2012) SED fitting. Zhang et al. (2016) detect a weak correlation (although their measurements are all within 1σ), such that stellar mass and halo mass are more strongly correlated at larger aperture radii, in agreement with observations of inside-out galaxy growth (e.g., van Dokkum et al. 2010). We investigate this trend by reintegrating the SDSS light profiles at fixed physical radii of 10, 20, 30, 40, 50, 60, 70, 80, 90, and 100 kpc for the 189 SDSS-C4 clusters with radial extents greater than 100 kpc from GM&M18 and measure the SMHM $-m_{\rm gap}$ relation at each radial extent. For each Bayesian MCMC analysis, we use the same $m_{\rm gap}$ from the Petrosian magnitudes and the caustic halo masses with reduced uncertainty. This analysis was performed using the Bayesian formalism described in Section 4, with the redshift parameters set to 0.0. Additionally, we do a second analysis where we set γ to 0.0. The results are shown in Figure 2 for both analyses. Figure 2 also shows the slope measured by Pillepich et al. (2018) for the Illustris TNG300 simulation, where stellar masses are determined using the SUBFIND algorithm to identify and sum the stellar particles bound to a galaxy within a fixed 3D physical radius.

The primary takeaway from Figure 2 is that the choice of radial extent within which the BCG's stellar mass is measured significantly impacts the SMHM relation's slope. This result confirms the idea presented by Zhang et al. (2016) and suggests that the outer halo of the BCG is indeed tied to the underlying parent (cluster) halo. Moreover, our result observationally confirms a trend suggested by the EMERGE empirical model (Moster et al. 2018). Moster et al. (2018) find that to match observational baryon conversion efficiencies at low redshifts, empirical models must incorporate a fraction of the ICL, since the baryon conversion efficiency of central galaxies (a proxy for stellar mass) in clusters at fixed halo mass is underapproximated

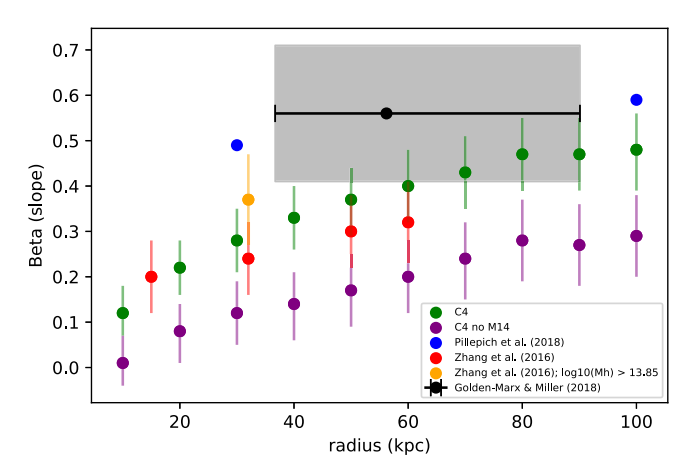


Figure 2. Slope of the SMHM relation as a function of the BCG's radial extent, where $m_{\rm gap}$ is incorporated (green) and when it is not (purple). The results of Zhang et al. (2016) are shown in red and yellow. The results from Pillepich et al. (2018) using ILLUSTRIS TNG300 are shown in blue. For comparison, the slope measurement from GM&M18 is shown in black with the gray bar. The radial range represents the median and standard deviations of the Petrosian radii for the SDSS-C4 sample. Measuring the stellar mass within a larger radial extent steepens the slope of the SMHM relation because the outer regions of BCGs are tied to the parent clusters. Additionally, incorporating M14 also steepens the slope, which is expected if M14 is related to BCG growth.

by empirical models when compared to observational results, which generally measure BCG stellar masses within larger radii than those used in empirical models. Thus, similar to our results, Moster et al. (2018) find that the conversion efficiency, at fixed halo mass, which is similar to the slope of the SMHM relation, increases when parts of what have been previously classified as ICL are included in the stellar mass estimate of the BCG.

This trend between slope and radial extent is important because previously published SMHM relations often use model magnitudes or state that their stellar masses are estimated within Kron or Petrosian radii, which, unless the specific radial extents are provided, can lead to a biased comparison between published results and an improper comparison between BCGs in large samples where those radii greatly differ. Additionally, the slope of the SMHM relation levels off around 80–100 kpc,

which shows that beyond this radial extent we gain no additional information. This result agrees with the analysis of Huang et al. (2018), who use Hyper Suprime Cam Subaru Strategic Program observations of massive galaxies over the redshift range 0.3 < z < 0.5 and find that the difference between the stellar mass within 100 kpc and the total stellar mass is on average ~ 0.02 dex. Moreover, Zhang et al. (2019), who use DES Year 1 observations to study the ICL surrounding BCGs in the redshift range 0.2 < z < 0.3, suggest that 100 kpc marks the transition region between the ICL and BCG. Therefore, our choice of a 100 kpc aperture for our BCG magnitudes accounts for the majority of the stellar mass in the BCG.

The second significant result we find is that the slope is statistically different depending on whether we use the latent $m_{\rm gap}$ and its stretch parameter in the SMHM relation. We found no significant difference in GM&M18 and attribute this to the use of the Petrosian magnitudes to estimate stellar masses. The Petrosian radius is a measured quantity that causes a blending of the underlying physical apertures depending on the BCG redshift. Therefore, not only does using a small aperture lead to a shallower slope, but the absence of accounting for the BCG's assembly history, via $m_{\rm gap}$, does as well.

At the largest radii, we find excellent agreement with the results from the ILLUSTRIS TNG300 simulation (Pillepich et al. 2018). Unlike the Guo et al. (2011) semi-analytic galaxy treatment, ILLUSTRIS TNG is a full hydrodynamic *N*-body simulation that contains the following astrophysical properties: gas cooling and photoionization, star formation within an interstellar medium, stellar evolution and feedback, and black holes with feedback.

5.2. Error Calibration

The deeper redMaPPer sample lacks good spectroscopic coverage, so we expect some issues with projection when measuring $m_{\rm gap}$. In GM&M18, we used $\sigma_{z_0}=0.1$ dex as our uncertainty in $m_{\rm gap}$, which is consistent with the 3D simulations for the spectroscopically complete low-redshift SDSS-C4 sample and the precision of our Petrosian magnitudes. We expect a slightly larger σ_{z_0} for the redMaPPer sample because the reduction of the photometric error in the BCG magnitudes is offset by issues such as projection effects and the $P_{\rm mem}$ criterion when determining $m_{\rm gap}$. However, we need to determine a reasonable value to use for σ_{z_0} for the redMaPPer sample in our Bayesian analysis.

In addition to the above issue, by employing a mass–richness relation, the Bayesian analysis requires the scatter in mass at fixed richness $\sigma(M|\lambda)$. To date, this quantity is not well constrained. Andreon (2015) report this scatter to be as low as $\sigma(\ln M_{200}|\lambda) < 0.05$ at 90% confidence. In contrast, Rozo et al. (2015) find a larger scatter of 0.17–0.21, depending on what they assume for the intrinsic scatter in cluster SZ-based masses and its covariance with the observed richness.

We begin the error calibration of the SDSS-C4 mass-richness scatter by conducting a simultaneous analysis of the SDSS-C4 SMHM relation using both the individual cluster caustic masses and the masses determined from the SDSS-C4 mass-richness relation. Regardless of the cluster mass used, we require the resultant parameters of the SMHM to agree within 1σ . In this analysis, we allow caustic mass errors $\sigma(M)_{\text{data}}$ to be a free parameter. The intrinsic scatter, $\sigma(M|\lambda)$, is then constrained by the observed scatter in the mass-richness

relation: $\sigma(M|\lambda)_{\rm obs}^2 = \sigma(M)_{\rm data}^2 + \sigma(M|\lambda)_{\rm intrinsic}^2$. Without the additional constraint from the SMHM relation, our inferred $\sigma(M|\lambda)$ would be fully degenerate with the unknown true errors on the observational measurements.

To ensure the completeness of the sample, we use only the 128 clusters with $\log_{10}(M_{\rm halo}/(h^{-1}M_{\odot})) > 14.0$, regardless of whether it is the dynamically inferred caustic mass or the richness-inferred mass. We find that $\sigma(\ln M_{200}|\mathcal{X}^{C4}) = 0.20^{+0.03}_{-0.04}$ (where \log_{10} and \ln refer to the log base 10 and natural log, respectively). At the same time, we find that the simulation-calibrated caustic errors provided in Gifford et al. (2013) are overestimated by $\sigma(\ln M_{200}) = 0.19$, on average. We note that we could have just chosen $\sigma(\ln M_{200}|\lambda) = 0.20$ (Rozo et al. 2015). However, the joint mass–richness and SMHM relation analysis suggests that $\sigma(\ln M_{200}|\lambda) \simeq 0.20$ is well motivated observationally. The full details of this analysis are beyond the scope of this work and can be found in C. J. Miller et al. (2019, in preparation). However, this analysis gives us a purely data-inferred constraint on the appropriate intrinsic mass–richness scatter to use for the SDSS-C4 sample.

We still need to estimate the intrinsic scatter in the redMaPPer mass–richness relation, as well as uncertainties in $m_{\rm gap}$ values and the stellar masses for the redMaPPer sample. We choose to calibrate the redMaPPer observational uncertainties, σ_{x_0} , σ_{y_0} , and σ_{z_0} , by defining a redMaPPer subsample that matches the SDSS-C4 redshift distribution function (down to z=0.081) and apply the richness-based mass limit $\log_{10}(M_{\rm halo}/(h^{-1}M_{\odot})) \geqslant 14.0$. With this new redMaPPer calibration sample, we treat σ_{x_0} , σ_{y_0} , and σ_{z_0} as nuisance parameters on a coarse grid in the Bayesian analysis and solve for their mean best values by requiring that the inferred slope, amplitude, stretch parameter, and intrinsic scatter of the redMaPPer calibration sample are within 1σ of the values found for the SDSS-C4 sample.

The posterior distributions for the calibration samples are given in lines 2 and 3 of Table 3. We find good agreement between the SDSS-C4 richness sample and the redMaPPer calibration sample for α , β , γ , and $\sigma_{\rm int}$ when the stellar mass uncertainties are $\sigma_{y_0} \simeq 0.08$ dex, the magnitude-gap uncertainties are $\sigma_{z_0} \simeq 0.15$, and the inferred intrinsic scatter in the mass–richness relation is $\sigma(\ln M_{200}|\lambda) = 0.20$, which corresponds to $\sigma_{x_0} = 0.087$ dex. The slope (β) and intrinsic scatter $\sigma_{\rm int}$ for the redMaPPer and SDSS-C4 low-redshift calibration samples are within 1σ of each other. The inferred stretch parameter γ and offset α differ between SDSS-C4 and redMaPPer by 1.5σ , and the redMaPPer value for γ is closer to the result presented for the caustic-based SDSS-C4 sample in GM&M18.

To match the results of the SDSS-C4 richness sample, we adjust some measurement uncertainties from the values used in GM&M18 for the SDSS-C4 sample. σ_{y_0} is the same for the SDSS-C4 and SDSS-redMaPPer samples since both have stellar masses estimated via EzGal (Mancone & Gonzalez 2012) using the SDSS 100 kpc BCG magnitudes. However, as previously discussed, this is a reduction from what was used in GM&M18, which is due to the von der Linden et al. (2007) corrected Petrosian magnitudes, which add uncertainty due to the background correction and measurement of Petrosian radii. σ_{z_0} is slightly larger, at 0.15 for the redMaPPer data owing to our concerns about projection effects and our high- $P_{\rm mem}$ criterion. Most importantly, σ_{x_0} is the same for the SDSS-C4 richness sample and the redMaPPer calibration sample, which highlights that despite using different mass-richness relations,

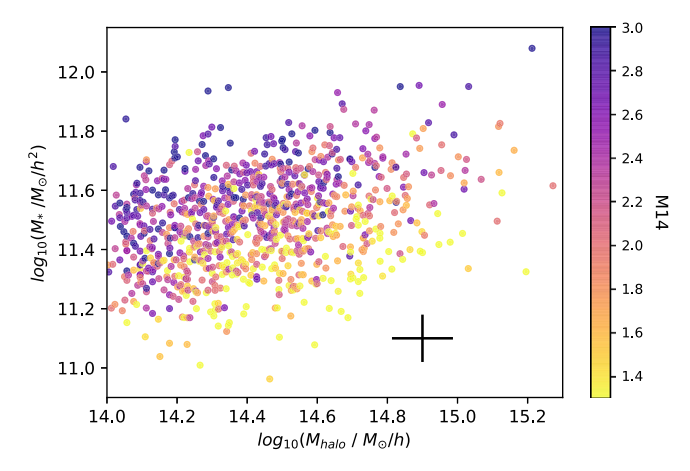


Figure 3. SMHM relation for the combined redMaPPer and SDSS-C4 clusters colored via M14. As in GM&M18, we see that a stellar mass– $m_{\rm gap}$ stratification exists at higher redshifts. The black plus sign represents the error in halo mass, 0.087 dex, and stellar mass. 0.08 dex.

the uncertainty associated with this mass estimate is relatively constant.

The above error calibration provides us with estimates of the uncertainties on the observables. The values we obtain are reasonable and in agreement with expectations. We do not have good estimates on the errors on these uncertainties in the observables. However, it is important to recall that Equation (8) does allow for uncertainty in the observed errors. So while we set an initial mean value using the techniques described in this subsection (i.e., σ_{x_0} , σ_{y_0} , σ_{z_0}), the observational errors applied in the Bayesian analysis are actually free (nuisance) parameters.

We make a final note that the subset used to calibrate the observable errors in the redshift overlap range between the SDSS-C4 and redMaPPer samples is different from the matched SDSS-C4/redMaPPer sample used to calibrate the redMaPPer membership probability threshold. These redMaPPer subsamples each serve their own purposes and differ to maximize the amount of usable data. However, once the errors are calibrated between SDSS-C4 and redMaPPer, we can use all available redMaPPer and C4 data in the final analysis over the redshift range $0.03 \leqslant z \leqslant 0.3$. Without this calibration, there could be underlying and unaccounted-for systematic uncertainties between the two baseline samples that would cloud the statistical inference.

6. Results

6.1. Combined redMaPPer and SDSS-C4 Results

In this section, we present the qualitative and quantitative results from our analysis of the C4 and redMaPPer data. We highlight the qualitative results of this study in Figure 3, which compares the stellar masses estimated using EzGal (Mancone & Gonzalez 2012) to the halo masses, estimated using the Simet et al. (2017) mass–richness relation. In addition, we include the 142 richness-selected SDSS-C4 clusters, bringing our total sample to 985 clusters. The color bar is based on the M14 values for each cluster. The data shown in Figure 3 encompass the redshift range $0.03 \le z \le 0.30$. Therefore, the stratification observed in our low-redshift SDSS-C4 sample (at fixed halo mass, as stellar mass increases, so does M14) exists at higher redshifts than observed in GM&M18. Furthermore, although not shown, when the sample is binned by redshift, the

stellar mass–M14 stratification also exists. Additionally, this stratification is present in the Guo et al. (2011) prescription of the Millennium Simulation at each of the discrete redshift snapshots discussed in Section 3.6.

We evaluate the impact of incorporating $m_{\rm gap}$ and redshift into the SMHM relation using our previously described MCMC model (Section 4), Bayesian formalism, and linear SMHM relation (Equation (7)). In Figure 4, we present a triangle plot that shows the 1D and 2D posterior distributions for each of the eight parameters, α , β , γ , n_1 , n_2 , n_3 , n_4 , and $\sigma_{\rm int}$. For this analysis, as well as the initial calibration analysis, we shifted the x- and y-axes to eliminate the covariance between α and β . To do this, we subtracted the median values of the halo mass and stellar mass of the combined SDSS-C4 richness and SDSS-redMaPPer samples: $x_{\rm med} = 14.41$ and $y_{\rm med} = 11.50$. The posterior results, as well as the posterior results when $m_{\rm gap}$ is not included, are presented in Table 2. The difference between these results is discussed in Section 7.

In Figure 4, excluding the original parameters and their associated redshift evolution parameters, only a few pairs of parameters are strongly covariant: α and γ , α and n_3 , γ and n_1 , and n_1 and n_3 . α and γ are covariant because of the shifted axis, which results in the location of α corresponding to where M14 = 0.0. Figure 4 illustrates that the primary results presented in GM&M18 still hold true; γ is definitively nonzero, $\sigma_{\rm int}$ is \sim 0.1 dex, and incorporating $m_{\rm gap}$ decreases $\sigma_{\rm int}$ by \sim 0.04 dex, or \approx 30%. We note that the error bars on the redMaPPer values are similar to those presented in GM&M18 because of the addition of the redshift evolution parameters.

The most important takeaway from Figure 4 is the significance of the redshift evolution parameter, n_2 , which is definitively nonzero. n_1 and n_3 are within 1σ of 0.0, while n_4 is slightly greater than 1σ from 0.0. n_2 is also the most interesting parameter because no covariance exists between n_2 and any parameter other than β , which signifies that for the first time we detect statistically significant (>3.5 σ) redshift evolution in the slope of the SMHM relation. To improve our understanding of our measurements of the redshift evolution of α and γ , we need to eliminate the covariance between these parameters, without reintroducing covariance with β .

To reach these results, we have devloped and implemented a detailed and careful analysis to ensure that the lower-redshift SDSS-C4 data and the higher-redshift SDSS-redMaPPer data are homogeneous. Specifically, we ensured that both data sets utilize the same underlying instrumentation (SDSS), the same underlying photometric detrending pipeline (SDSS), the same underlying spectroscopic pipeline (SDSS), the same physical fixed-aperture photometry for all BCGs, the same cluster galaxy membership to define the magnitude gap (as discussed in Section 3.1), the same algorithm and parameters to determine the stellar masses, the same mass-richness technique to infer cluster masses, the same cluster masses in the overlap sample (to within errors), and the same algorithm to measure completeness criteria defining the underlying cluster samples in both $m_{\rm gap}$ and cluster mass. However, it is possible that there is still some systematic error that we have missed in the SDSS-C4 sample that is dominating the evolution in the slope. The best we can do is remove this data set from our Bayesian analysis, even though it is the only available data set complete below z < 0.10, thus limiting our ability to track late-time evolution in the SMHM relation. We list the inferred parameters without the SDSS-C4 data in Table 2. The parameters are within 1σ for

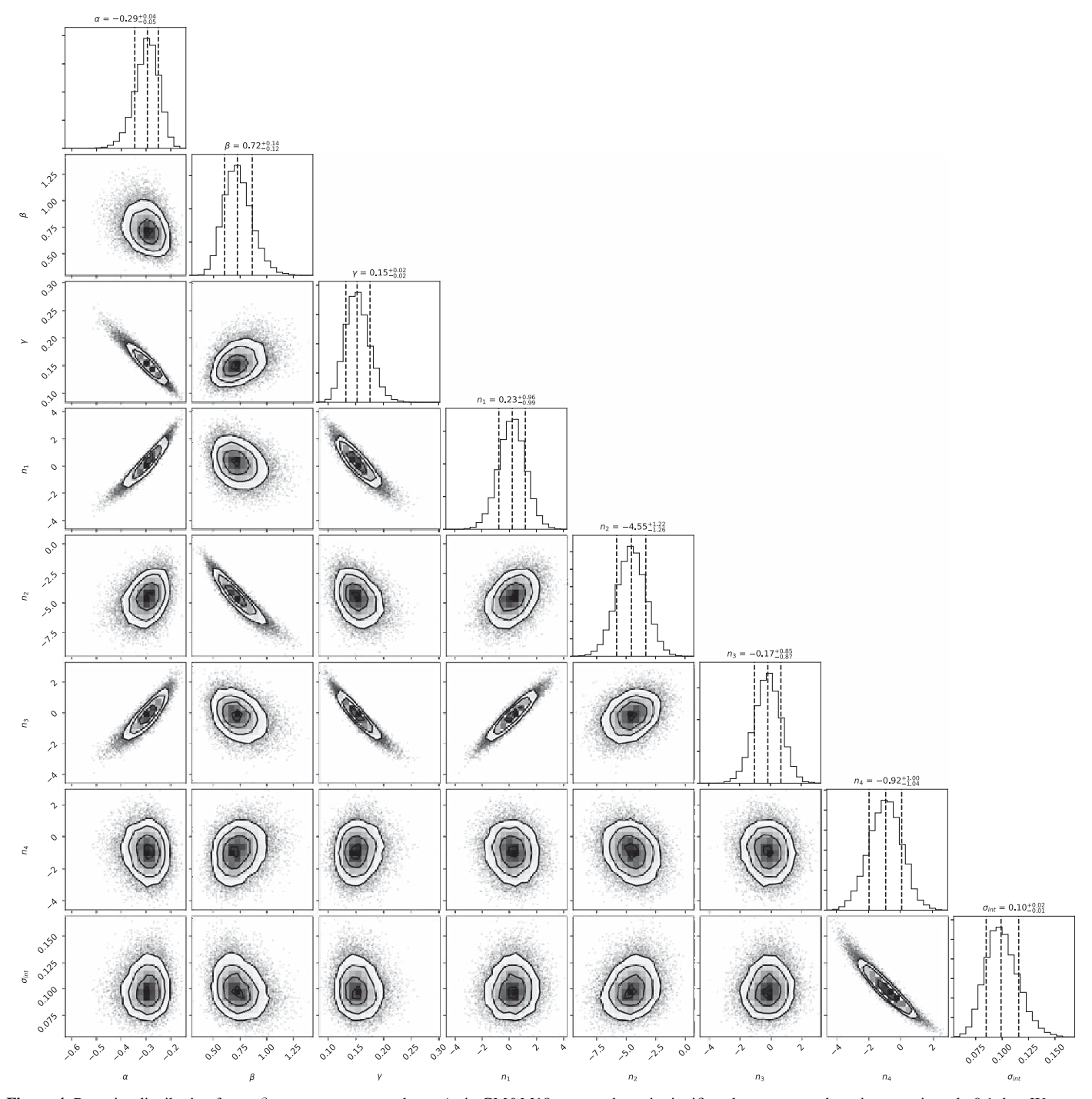


Figure 4. Posterior distribution for α , β , γ , n_1 , n_2 , n_3 , n_4 , and σ_{int} . As in GM&M18, we see that γ is significantly nonzero and σ_{int} is approximately 0.1 dex. We note that the posteriors measured here are extrapolations out to redshift = 0.0. To see the values at the redshifts measured in our study, see Figures 5–8. The redshift parameter n_2 is the only parameter that is significantly nonzero. Therefore, some, albeit weak, redshift evolution in the slope of the SMHM relation can be detected over $0.03 \le z \le 0.3$.

 α , β , σ_{int} , n_1 , n_2 , and n_4 , while γ and n_3 are within 1.5 σ . After dropping the SDSS-C4 data, we still find evolution in the slope, albeit at a slightly lower (as expected) statistical significance (99% versus 99.9% when including SDSS-C4). Therefore, we conclude that while including the C4 data strengthens our detection, it is not responsible for it. We conduct a similar analysis by dropping the highest-redshift cluster data (line 5 of Table 2). We find the evolution at a slightly higher significance (99.98%). Thus, we argue that the significance of the detection

in the evolution of the slope is fairly robust to the upper and lower ends of the redshift distribution of our data.

6.2. Comparison to Simulations and Binned Results

Here we compare the trends shown for the binned SDSS-redMaPPer clusters to those measured in the Guo et al. (2011) prescription of the Millennium Simulation. The results for each of the measured parameters, α , β , γ , and $\sigma_{\rm int}$, are presented in

 Table 2

 Posterior Distribution Results with Redshift Evolution

Data	$\alpha(z=0)$	$\beta(z=0)$	$\gamma(z=0)$	$\sigma_{\rm int}(z=0)$	n_1	n_2	n_3	n_4
With M14	$-0.29^{+0.04}_{-0.05}$	$0.72^{+0.14}_{-0.12}$	0.15 ± 0.02	$0.099^{+0.017}_{-0.014}$	$0.23^{+0.96}_{-0.99}$	$-4.55^{+1.22}_{-1.26}$	$-0.17^{+0.85}_{-0.87}$	$-0.92^{+1.00}_{-1.04}$
Without M14	$0.14^{+0.03}_{-0.02}$	$0.37^{+0.13}_{-0.10}$	•••	$0.142^{+0.016}_{-0.014}$	$-2.03^{+1.27}_{-1.22}$	$-2.25^{+1.86}_{-1.96}$	•••	$-0.68^{+0.67}_{-0.68}$
With $M_{\rm halo}$ C4 shifted	$-0.31^{+0.05}_{-0.06}$	$0.72^{+0.15}_{-0.14}$	0.14 ± 0.02	$0.109^{+0.017}_{-0.015}$	$0.03^{+1.08}_{-1.09}$	$-4.98^{+1.41}_{-1.39}$	$0.41^{+0.90}_{-0.94}$	$-1.49^{+1.00}_{-0.96}$
Without C4	$-0.44^{+0.07}_{-0.09}$	$0.60^{+0.13}_{-0.11}$	0.23 ± 0.04	$0.100^{+0.021}_{-0.017}$	$-1.67^{+1.12}_{-1.16}$	$-2.95^{+1.26}_{-1.35}$	$-2.53^{+1.01}_{-1.07}$	$-1.07^{+1.13}_{-1.15}$
Without M14 and C4	$0.18^{+0.06}_{-0.04}$	$0.25^{+0.08}_{-0.06}$	•••	$0.149^{+0.019}_{-0.017}$	$-4.92^{+1.90}_{-1.99}$	$0.84^{+1.61}_{-1.66}$	•••	$-1.09^{+0.77}_{-0.74}$
Without $z > 0.25$	-0.34 ± 0.06	$0.75^{+0.16}_{-0.13}$	$0.17^{+0.03}_{-0.02}$	$0.108^{+0.018}_{-0.016}$	$-0.55^{+1.17}_{-1.16}$	$-5.09^{+1.43}_{-1.42}$	$-0.81^{+1.02}_{-1.00}$	$-1.44^{+1.10}_{-1.13}$

 Table 3

 Posterior Distribution Results

Data	z_{min}	z_{max}	z_{med}	$\log_{10}(M_{\rm halo}/(h^{-1}M_{\odot}))_{\rm min}$	$n_{ m clusters}$	$\alpha(z=z_{\rm med})$	$\beta(z=z_{\rm med})$	$\gamma(z=z_{\rm med})$	$\sigma_{\rm int}(z=z_{\rm med})$
GM&M18	0.030	0.151	0.086	14.0	236	3.13 ± 2.09	0.56 ± 0.15	0.173 ± 0.022	0.085 ± 0.024
SDSS-C4 richness	0.030	0.146	0.081	14.0	142	-0.23 ± 0.05	0.52 ± 0.08	0.122 ± 0.019	0.098 ± 0.012
redMaPPer calibration	0.081	0.146	0.098	14.0	70	-0.40 ± 0.06	0.48 ± 0.13	0.190 ± 0.024	0.087 ± 0.017
redMaPPer	0.081	0.135	0.113	14.00	222	-0.38 ± 0.04	0.42 ± 0.05	0.182 ± 0.016	0.092 ± 0.009
redMaPPer	0.135	0.169	0.153	14.06	208	-0.34 ± 0.03	0.44 ± 0.05	0.168 ± 0.014	0.068 ± 0.009
redMaPPer	0.169	0.208	0.184	14.17	203	-0.29 ± 0.03	0.30 ± 0.06	0.131 ± 0.015	0.087 ± 0.008
redMaPPer	0.208	0.300	0.247	14.39	210	-0.34 ± 0.03	0.32 ± 0.06	0.150 ± 0.013	0.082 ± 0.009
Guo et al. (2011)	0.089	0.089	0.089	14.00	815	-0.34 ± 0.01	0.44 ± 0.02	0.226 ± 0.006	0.093 ± 0.002
Guo et al. (2011)	0.116	0.116	0.116	14.00	458	-0.37 ± 0.02	0.45 ± 0.02	0.230 ± 0.008	0.093 ± 0.003
Guo et al. (2011)	0.144	0.144	0.144	14.06	212	-0.36 ± 0.03	0.45 ± 0.03	0.229 ± 0.014	0.105 ± 0.005
Guo et al. (2011)	0.175	0.175	0.175	14.17	199	-0.32 ± 0.02	0.41 ± 0.04	0.207 ± 0.011	0.089 ± 0.005
Guo et al. (2011)	0.242	0.242	0.242	14.39	42	-0.33 ± 0.06	0.33 ± 0.08	0.224 ± 0.025	0.089 ± 0.011

Note. The Guo et al. (2011) data have the same z_{min} and z_{max} because these are data analyzed at individual snapshots, not data from a light cone.

Table 3. For a more accurate comparison, the Guo et al. (2011) measurements are taken on data samples described in Section 3.6. Due to the limits of the Guo et al. (2011) prescription, using the halo mass distribution functions from the SDSS-redMaPPer data significantly decreases the number of clusters, particularly in the higher-redshift simulation boxes, resulting in larger posterior uncertainties. To illustrate the trends we observe in Tables 2 and 3, in Figures 5–8 we present the redshift evolution of the offset (α) , slope (β) , stretch factor (γ) , and intrinsic scatter $(\sigma_{\rm int})$, respectively, given by the posterior distributions shown in Figure 4.

Figure 6 illustrates that our redshift-dependent Bayesian MCMC model finds that the slope of the SMHM relation decreases with increasing redshift for the combined SDSS-C4 and SDSS-redMaPPer clusters. In contrast, Figures 5, 7, and 8 illustrate that, using our Bayesian MCMC model, we observe either no or weak redshift evolution in the amplitude, in agreement with the results from Zhang et al. (2016), $m_{\rm gap}$ stretch parameter, and intrinsic scatter. Interestingly, the SDSSredMaPPer data (blue points) for each of the four measured parameters and the Guo et al. (2011) Millennium Simulation measurements show similar trends in how each parameter varies with redshift. Since the Guo et al. (2011) prescription of the Millennium Simulation is modeled to look like the SDSS observational data, this is likely an artifact of the semi-analytic modeling. We discuss the meaning of these redshift evolution parameters in the context of hierarchical growth in Section 7.

6.3. Comparison to Golden-Marx & Miller (2018) Results

The use of the richness-based masses compared to caustic-based masses reduces the uncertainties on the SMHM parameters, even for the smaller sample size. The offset α is different from the value presented in GM&M18 because we use

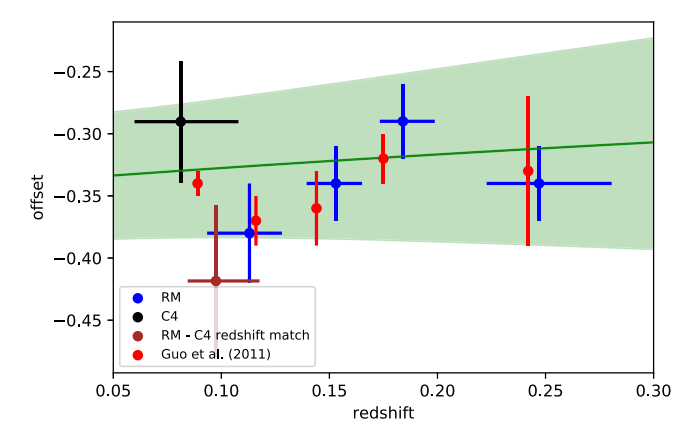


Figure 5. Binned offsets and respective error bars plotted as a function of redshift for the SDSS-redMaPPer binned and calibration samples, SDSS-C4 richness sample, and the Guo et al. (2011) prescription of the Millennium Simulation. The green line represents the redshift evolution suggested from the posterior results presented in Figure 4. The green shaded region represents the combined total error from uncertainty on n_1 and α . This comparison highlights that the offset of the SMHM relation does not evolve over the redshift range $0.03 \leqslant z_{\rm red} \leqslant 0.3$.

a different method to estimate stellar mass, as discussed earlier, and have offset the axes by subtracting the median values of the stellar mass and halo mass. The slope (β) and the intrinsic scatter $(\sigma_{\rm int})$ are statistically the same (within 1σ). The inferred stretch parameter γ is smaller (by $\sim 1.5\sigma$) in the richness-based SDSS-C4 SMHM relation, but still significantly nonzero. Therefore, the conclusions from GM&M18 hold when we switch to using richness-based masses for the SDSS-C4 sample. The measured posteriors for the entire SDSS-C4 richness sample (containing 142 clusters) can be found in Table 3 and agree with the posteriors for the calibration sample containing 128 clusters.

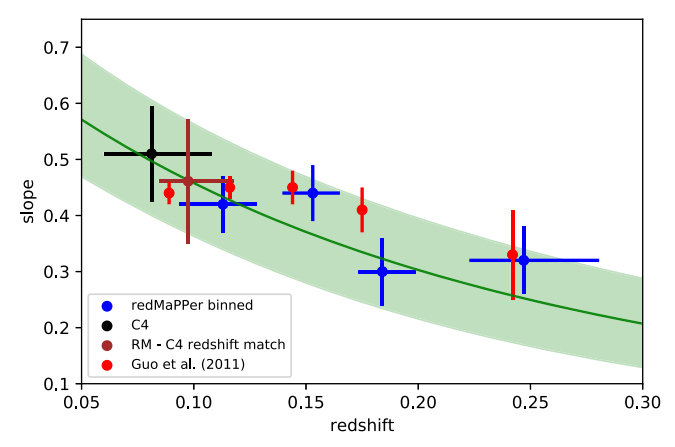


Figure 6. Binned slopes and respective error bars plotted as a function of redshift for SDSS-redMaPPer binned and calibration samples and the Guo et al. (2011) prescription of the Millennium Simulation. The green line represents the redshift evolution suggested from the posterior results presented in Figure 4. The green shaded region represents the combined total error from uncertainty on n_2 and β . This comparison highlights that the slope of the SMHM relation evolves over the redshift range $0.03 \le z_{\rm red} \le 0.3$.

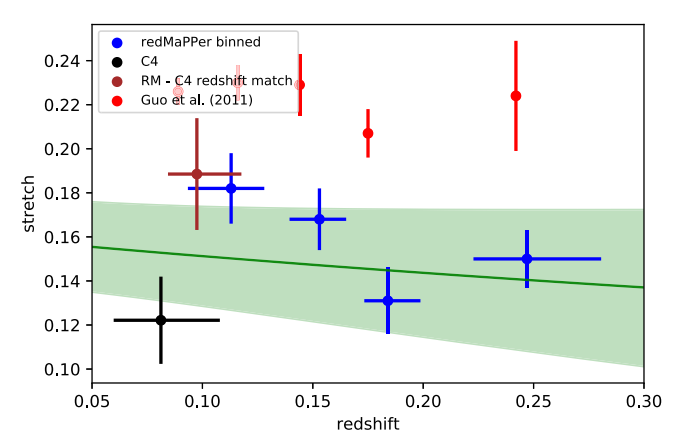


Figure 7. Binned stretch factors and respective error bars plotted as a function of redshift for the SDSS-redMaPPer binned and calibration samples, SDSS-C4 richness sample, and Guo et al. (2011) prescription of the Millennium Simulation. The green line represents the redshift evolution suggested from the posterior results presented in Figure 4. The green shaded region represents the total error incorporating both the uncertainty on n_3 and γ . This trend highlights that there is no redshift evolution in γ in this redshift range.

7. Discussion

The change of the SMHM relation's slope and $\sigma_{\rm int}$ can tell us about central galaxy hierarchical growth. In semi-analytic models (SAMs), some researchers find stellar mass growth in BCGs at late times. Between the redshift range z=0.5 and z=0.0, De Lucia & Blaizot (2007) find that BCG stellar mass increases by a factor of 2, Shankar et al. (2015) find a growth factor of 1.5, and Guo et al. (2011) measure an increase in stellar mass by a factor of 1.9. The effect of BCG growth in Guo et al. (2011) can be seen on the slope of the SMHM in Figure 6, which decreases by $\sim 30\%$ out to z=0.3.

In this work, we extended our study of the cluster-scale SMHM relation to $z_{\rm red} = 0.3$. By incorporating the stretch parameter and $m_{\rm gap}$, we reduce $\sigma_{\rm int}$ and the uncertainty on the slope in the SMHM relation, allowing us to observe redshift evolution. As shown in Table 2, when $m_{\rm gap}$ information is not incorporated, we measure a much weaker redshift evolution parameter, n_2 , for the slope. Instead of a >3.5 σ detection, we

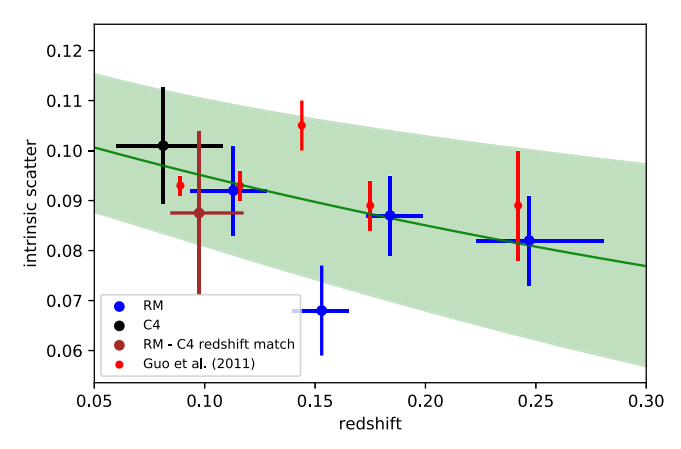


Figure 8. Binned stretch factors and respective error bars plotted as a function of redshift for the SDSS-redMaPPer binned and calibration samples and Guo et al. (2011) prescription of the Millennium Simulation. The green line represents the redshift evolution suggested from the posterior results presented in Figure 4. The green shaded region represents the total error incorporating both the uncertainty on n_4 and $\sigma_{\rm int}$. This trend highlights that there is weak redshift evolution in $\sigma_{\rm int}$.

measure a $<1.5\sigma$ detection for n_2 if the C4 data are included and no detection when they are not. Therefore, it is only when incorporating $m_{\rm gap}$ that we see that the slope of the SMHM relation evolves over the redshift range $0.03 \le z \le 0.3$. Thus, environment strongly impacts the SMHM relation.

One can interpret the observed redshift evolution in the SMHM relation's slope in the context of results from Gu et al. (2016). When BCGs grow hierarchically, their stellar mass increases owing to major and minor mergers. Gu et al. (2016) suggest that the steepening of the slope is related to σ_{int} , such that an increase in the $\sigma_{\rm int}$ corresponds to an increase in the slope and that the slope and σ_{int} are tied to the progenitor history of the BCG such that a wider range of progenitor galaxies yield a steeper slope and a larger σ_{int} . Additionally, a steeper SMHM relation results from a growth history where minor mergers dominate over major mergers. Moreover, the late-time evolution in the slope we observe suggests that the BCGs residing in more massive halos undergo a greater growth over this period of time than those in less massive halos, which may result from differences in the galactic populations of highand low-mass cluster halos.

In Figure 6, the Guo et al. (2011) SAMs show a similar decrease in the slope over the redshift range $0.03 \le z \le 0.3$. The similarity in this trend between the observations and simulations is interesting because other observational studies do not find a similar result (Oliva-Altamirano et al. 2014; Gozaliasl et al. 2016). This discrepancy was previously justified because the continued growth in simulations is in the stellar mass of BCG cores and not in the outer portion of BCG envelopes, the ICL (Zhang et al. 2016), as is observed (van Dokkum et al. 2010; Burke et al. 2015). However, by comparing the stellar masses measured within a radial extent of 100 kpc, we are not analyzing just the inner profile of the BCG, which is relatively constant over this redshift range (van Dokkum et al. 2010); instead, we are incorporating many of the radial regimes that have been previously treated as ICL. Therefore, the novelty of our detected evolution over the redshift range 0.03 < z < 0.30 likely results from our choice to measure the BCG stellar mass within a large radial extent, which incorporates the radial regions where BCGs actively grow, and the incorporation of $m_{\rm gap}$, as previously discussed.

Our results also allow us to comment on the absence of a trend in the evolution of the $m_{\rm gap}$ stretch parameter over this redshift range, as shown in Figure 7. This can be interpreted as meaning that with respect to stellar mass, $m_{\rm gap}$ is constant. The lack of redshift evolution of γ in our data is expected because even though $m_{\rm gap}$ and stellar mass growth are correlated, since our stellar mass measurement accounts for the outer portion of the BCG, it likely accounts for any recent merger material that may change either $m_{\rm gap}$ or the stellar mass. If γ were to decrease with redshift, it means that as we move forward in time, $m_{\rm gap}$ increases with respect to the stellar mass. This would occur if the BCGs were to have mergers with brighter galaxies in the given redshift range and the resulting additional mass were to go predominately to stellar mass located in the outer envelope of the BCGs (in our case at radii greater than 100 kpc). However, while stellar material from a merger is ejected into the ICL, major mergers involving the brightest galaxies are not common for BCGs in this redshift range (Burke et al. 2015).

Since the growth in $m_{\rm gap}$ depends on BCG growth (Solanes et al. 2016), our results suggest that $m_{\rm gap}$ values for BCGs at $z\approx 1$ would be much lower (although γ may not change). Furthermore, if in fact both stellar mass and $m_{\rm gap}$ continue to decrease at these higher redshifts, in agreement with hierarchical growth, then we may be able to enhance this analysis and better constrain the redshift evolution of the parameters of our SMHM relation if we extend our analysis out to redshifts of $z\geqslant 0.5$. This can be tested in simulations using current SAMs that follow the growth history of the BCG (e.g., Guo et al. 2011), where these models have better agreement with observations (e.g., Lidman et al. 2012; Lin et al. 2013).

The observational challenge of extending our analysis of the SMHM– $m_{\rm gap}$ relation out to higher redshifts is to acquire good spectroscopic coverage for each cluster, again understand the additional systematic errors that increase the error associated with the photometric data used in each of the observed measurements in our SMHM relation, and have deep enough photometry to measure the BCG light profiles out to large radial extents.

The authors would like to thank the anonymous referee for their useful feedback on this paper. Additionally, the authors would like to thank Juliette Becker for help with the statistical analysis; Emmet Golden-Marx for useful discussions, help with the error analysis, and for reviewing a draft of this paper; and Yuanyuan Zhang for useful discussions and for reviewing a draft of this paper.

This material is based upon work supported by the National Science Foundation under Grant No. 1812739. The Millennium Simulation databases used in this paper and the web application providing online access to them were constructed as part of the activities of the German Astrophysical Virtual Observatory (GAVO). Funding for SDSS-III has been provided by the Alfred P. Sloan Foundation, the Participating Institutions, the National Science Foundation, and the U.S. Department of Energy Office of Science. The SDSS-III website is http://www.sdss3.org/.

SDSS-III is managed by the Astrophysical Research Consortium for the Participating Institutions of the SDSS-III Collaboration, including the University of Arizona, the Brazilian Participation Group, Brookhaven National Laboratory, Carnegie Mellon University, University of Florida, the French Participation Group, the German Participation Group, Harvard University, the Instituto de Astrofisica de Canarias, the Michigan State/Notre Dame/JINA Participation Group, Johns Hopkins University, Lawrence Berkeley National Laboratory, Max Planck Institute for Astrophysics, Max Planck Institute for Extraterrestrial Physics, New Mexico State University, New York University, Ohio State University, Pennsylvania State University, University of Portsmouth, Princeton University, the Spanish Participation Group, University of Tokyo, University of Utah, Vanderbilt University, University of Virginia, University of Washington, and Yale University.

ORCID iDs

Jesse B. Golden-Marx https://orcid.org/0000-0002-6394-045X

References

```
Aguerri, J. A. L., Girardi, M., Boschin, W., et al. 2011, A&A, 527, A143
Aihara, H., Allende Prieto, C., An, D., et al. 2011, ApJS, 195, 26
Alam, S., Albareti, F. D., Allende Prieto, C., et al. 2015, ApJS, 219, 12
Andreon, S. 2015, A&A, 582, A100
Andreon, S., & Hurn, M. A. 2010, MNRAS, 404, 1922
Behroozi, P., Wechsler, R., Hearin, A., & Conroy, C. 2019, MNRAS, in press
Behroozi, P. S., Wechsler, R. H., & Conroy, C. 2013, ApJ, 770, 57
Bell, E. F., McIntosh, D. H., Katz, N., & Weinberg, M. D. 2003, ApJL,
  585, L117
Bernardi, M., Hyde, J. B., Sheth, R. K., Miller, C. J., & Nichol, R. C. 2007, AJ,
  133, 1741
Bernardi, M., Meert, A., Sheth, R. K., et al. 2013, MNRAS, 436, 697
Brough, S., Tran, K.-V., Sharp, R. G., von der Linden, A., & Couch, W. J.
  2011, MNRAS, 414, L80
Bruzual, G., & Charlot, S. 2003, MNRAS, 344, 1000
Burke, C., Hilton, M., & Collins, C. 2015, MNRAS, 449, 2353
Colless, M. 1989, MNRAS, 237, 799
Croton, D. J., Springel, V., White, S. D. M., et al. 2006, MNRAS, 365, 11
Dariush, A. A., Raychaudhury, S., Ponman, T. J., et al. 2010, MNRAS,
  405, 1873
De Lucia, G., & Blaizot, J. 2007, MNRAS, 375, 2
Foreman-Mackey, D., Hogg, D. W., Lang, D., & Goodman, J. 2013, PASP,
   125, 306
Garilli, B., Maccagni, D., & Andreon, S. 1999, A&A, 342, 408
Gifford, D., Miller, C., & Kern, N. 2013, ApJ, 773, 116
Golden-Marx, J. B., & Miller, C. J. 2018, ApJ, 860, 2
Gozaliasl, G., Finoguenov, A., Khosroshahi, H. G., et al. 2016, MNRAS,
  458, 2762
Groenewald, D. N., Skelton, R. E., Gilbank, D. G., & Loubser, S. I. 2017,
  MNRAS, 467, 4101
Gu, M., Conroy, C., & Behroozi, P. 2016, ApJ, 833, 2
Guo, Q., White, S., Boylan-Kolchin, M., et al. 2011, MNRAS, 413, 101
Harrison, C. D., Miller, C. J., Richards, J. W., et al. 2012, ApJ, 752, 12
Henriques, B. M. B., White, S. D. M., Lemson, G., et al. 2012, MNRAS,
  421, 2904
Huang, S., Leauthaud, A., Greene, J. E., et al. 2018, MNRAS, 475, 3348
Jones, C., & Forman, W. 1984, ApJ, 276, 38
Jones, L. R., Ponman, T. J., & Forbes, D. A. 2000, MNRAS, 312, 139
Jones, L. R., Ponman, T. J., Horton, A., et al. 2003, MNRAS, 343, 627
La Barbera, F., de Carvalho, R. R., de La Rosa, I. G., et al. 2010, MNRAS,
  408, 1313
Lauer, T. R., Faber, S. M., Richstone, D., et al. 2007, ApJ, 662, 808
Lauer, T. R., Postman, M., Strauss, M. A., Graves, G. J., & Chisari, N. E. 2014,
   ApJ, 797, 82
Lidman, C., Suherli, J., Muzzin, A., et al. 2012, MNRAS, 427, 550
Lin, Y.-T., Brodwin, M., Gonzalez, A. H., et al. 2013, ApJ, 771, 61
Lin, Y.-T., & Mohr, J. J. 2004, ApJ, 617, 879
Mancone, C. L., & Gonzalez, A. H. 2012, PASP, 124, 606
Matthee, J., Schaye, J., Crain, R. A., et al. 2017, MNRAS, 465, 2381
Miller, C. J., Nichol, R. C., Reichart, D., et al. 2005, AJ, 130, 968
Moster, B. P., Naab, T., & White, S. D. M. 2013, MNRAS, 428, 3121
Moster, B. P., Naab, T., & White, S. D. M. 2018, MNRAS, 477, 1822
Oliva-Altamirano, P., Brough, S., Lidman, C., et al. 2014, MNRAS, 440, 762
```

```
Oser, L., Ostriker, J. P., Naab, T., Johansson, P. H., & Burkert, A. 2010, ApJ, 725, 2312

Pillepich, A., Nelson, D., Hernquist, L., et al. 2018, MNRAS, 475, 648

Proctor, R. N., de Oliveira, C. M., Dupke, R., et al. 2011, MNRAS, 418, 2054
Rhee, G. F. R. N., & Latour, H. J. 1991, A&A, 243, 38

Rozo, E., Rykoff, E. S., Bartlett, J. G., & Melin, J.-B. 2015, MNRAS, 450, 592

Rykoff, E. S., Rozo, E., Busha, M. T., et al. 2014, ApJ, 785, 104

Salpeter, E. E. 1955, ApJ, 121, 161

Schombert, J. M. 1986, ApJS, 60, 603

Shankar, F., Buchan, S., Rettura, A., et al. 2015, ApJ, 802, 73

Simet, M., McClintock, T., Mandelbaum, R., et al. 2017, MNRAS, 466, 3103
```

Solanes, J. M., Perea, J. D., Darriba, L., et al. 2016, MNRAS, 461, 321

```
Springel, V., White, S. D. M., Jenkins, A., et al. 2005, Natur, 435, 629
Tinker, J. L. 2017, MNRAS, 467, 3533
Tonini, C., Bernyk, M., Croton, D., Maraston, C., & Thomas, D. 2012, ApJ, 759, 43
Trevisan, M., Mamon, G. A., & Khosroshahi, H. G. 2017, MNRAS, 464, 4593
van Dokkum, P. G., Whitaker, K. E., Brammer, G., et al. 2010, ApJ, 709, 1018
von der Linden, A., Best, P. N., Kauffmann, G., & White, S. D. M. 2007, MNRAS, 379, 867
White, S. D. M., & Rees, M. J. 1978, MNRAS, 183, 341
Zhang, Y., Miller, C., McKay, T., et al. 2016, ApJ, 816, 98
```

Zhang, Y., Yanny, B., Palmese, A., et al. 2019, ApJ, 874, 165